JACS
JOURNAL OF THE AMERICAN CHEMICAL SOCIETY
pubs.acs.org/JACS

Article

Heterointercalation in Chevrel-Phase Sulfides: A Model Periodic Solid for the Investigation of Chain Electron Transfer

Konstantina G. Mason, Natalia Mosqueda, S. Avery Vigil, Paola N. Del Pozo-Gonzalez, Saxton Feiner, Kingston P. Robinson, Jenna M. Ynzunza, Ankita Kumari, Rose E. Smiley, Erika La Plante, George Agbeworvi, Ivan A. Moreno-Hernandez, and Jesús M. Velázquez*

Cite This: J. Am. Chem. Soc. 2025, 147, 18155−18165

Read Online

ACCESS | Metrics & More | Article Recommendations | Supporting Information

ABSTRACT: Modulation of electron density localization on periodic crystal solids through electron transfer from interstitial cations can directly influence the bonding configurations of small-molecule intermediates at the catalyst binding site. This study presents the microwave-assisted solid-state synthesis of four heterointercalant Chevrel-phase (CP) sulfides with varying metal cation intercalants with compositional and electronic structure investigations of the electron density redistribution as a result of intercalation. The heterointercalant CP sulfides, with the general formula $Cu_xM_yMo_6S_8$ (where M = Cr, Mn, Fe, Ni; x, y = 1.5−2.5), are presented here for the probe reaction of electrochemical CO_2 reduction. A change in product selectivity is observed toward the production of methanol at low overpotentials of −0.5 V vs reversible hydrogen electrode (RHE), as a result of the intercalant combination present within the CP interstitial cavity. Structural confirmation of all materials was examined through Rietveld refinement of the powder X-ray diffraction (PXRD) data, high-resolution transmission electron microscopy (HR-TEM), and selected-area electron diffraction (SAED). Electron transfer from the intercalated metal cations to the Mo_6S_8 cluster was investigated via X-ray photoelectron spectroscopy (XPS) of the intercalated metal cations and the chalcogenide cluster. Electron transfer was further confirmed through X-ray absorption analysis (XAS) of the K-edges of Mo and intercalants. Intermediate studies of electrochemical reduction of formaldehyde to methanol resulted in a faradaic efficiency of ∼78% methanol production on $Cu_xNi_yMo_6S_8$. The results presented herein identify distinct principles for materials design that can be utilized in other compositional spaces within the broad families of periodic crystal solids.

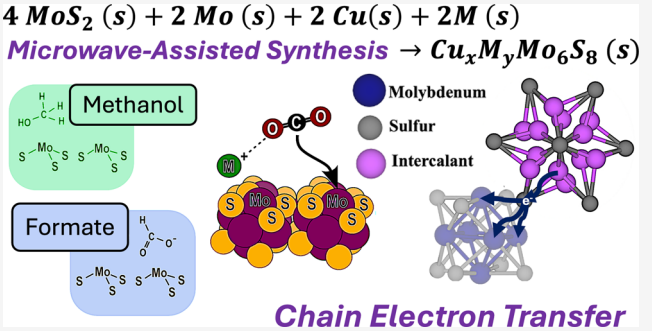

INTRODUCTION

The world's reliance on fossil fuels as a primary energy source has led to an exponential increase of atmospheric carbon dioxide (CO_2) in recent years. This has resulted in worldwide health effects and damages to countless ecosystems.[1,2] Utilization of renewable energy from sources such as solar and wind, to electrochemically reduce the captured CO_2 to liquid fuels such as methanol, must be investigated as an alternative to fossil fuel usage.[3] However, the existing electrochemical CO_2 reduction (CO_2R) relies on expensive noble-metal catalysts. Therefore, inexpensive, earth-abundant electrocatalysts capable of selective CO_2 reduction must be designed and implemented. Understanding the effects of compositional, structural, and electronic modifications on the electrocatalytic properties of periodic crystal solids is essential for advancing the design principles of electrocatalyst materials.[4] Specifically, a fundamental understanding of electron density redistribution as a result of electron transfer phenomena across catalyst frameworks can be utilized to modulate reaction trajectories through binding strengths and configurations.[5,6] Extended periodic solids, capable of hosting various metal cations within structured interstitial cavities, can be utilized to investigate electron density donation and redistribution through the presence of interstitial cations.[7]

An extended periodic solid characterized by its rhombohedral crystal symmetry and cubic cavity architectures is the Chevrel-phase (CP). Chevrel-phases, with the general formula $M_yMo_6T_8$ (where M = Group I, II, transition metals (TM), post-TM, or lanthanides; T = S, Se, Te; y = 0−4), are a class of materials comprised of a molybdenum octahedron encompassed by a pseudo-cubic chalcogen framework (T_8) and interconnected through bridging chalcogens, giving rise to an extended periodic solid (Figure 1a).[8] Originally, CP solids

Received: March 16, 2025
Revised: April 30, 2025
Accepted: May 5, 2025
Published: May 15, 2025

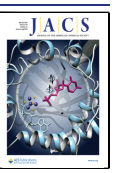

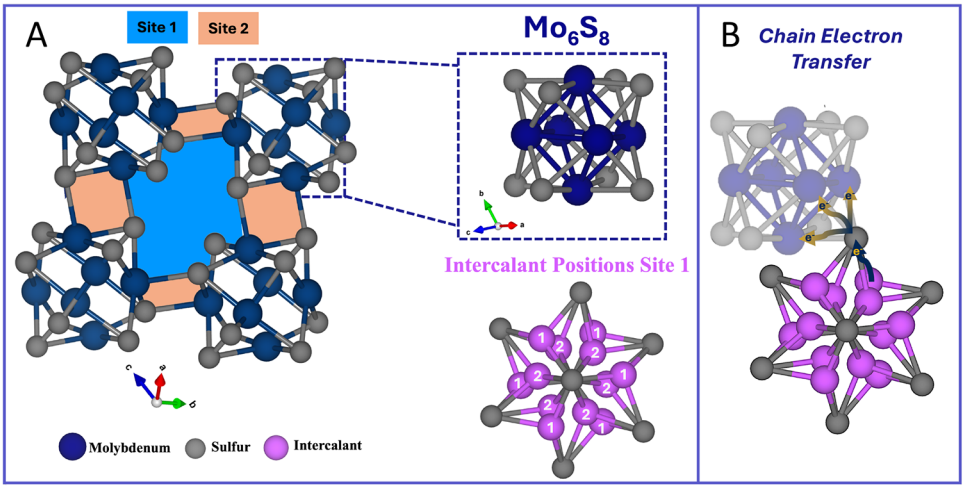

Figure 1. Structural representation of the extended Chevrel-phase periodic solid with individual cluster units of Mo_6S_8 and intercalant positions. Within each cavity, 12 equiprobable positions that can be occupied exist (intercalant positions site 1). The positions are further separated into "ring" designations based on the distance of the intercalant from the center of the cavity, which are numbers 1 or 2. Cations with a radius larger than 1 Å reside in the center of the cavity, while smaller cations, with a radius less than 1 Å, prefer to delocalize to the inner and outer ring positions due to favorable electrostatic interactions with the surrounding clusters (A). Representation of the proposed chain electron transfer mechanism in which the electron density is redistributed from the intercalant (purple) to the sulfur atoms at the corners of the Mo_6S_8 clusters (gray) to the Mo_6 octahedron (blue) (B).

were investigated for their applications as superconductors; however, they have repeatedly shown promise as multivalent battery cathode materials, thermoelectrics, and electrocatalysts.[9−19] Furthermore, the CP compositional space remains severely underexplored for electrochemical small-molecule catalysis, despite the unique presence of cavity architectures capable of hosting multiple metal cations with the potential to indirectly and directly influence catalytic properties through electron density donation (ligand effect) or electrostatic stabilization of intermediate species (ensemble effect).[17,19,20] CP materials exhibit high structural tunability through the intercalation of various metal cations into the cavity architectures formed by the interconnected Mo_6S_8 cluster units (Figure 1a). The primarily accessed cavity architecture, site 1 (shaded in blue in Figure 1a), is characterized by a pseudo-cubic structure formed by eight surrounding clusters and can host Type I (radius > 1Å) and Type II cations (radius < 1 Å).[21] The larger Type I cations are located at the origin of the cavity, equidistant from the surrounding clusters; however, smaller Type II cations delocalize between 12 inner and outer ring positions (intercalant positions site 1 shown in Figure 1a). An additional, much smaller cavity resides directly between two adjacent cluster units (shaded in orange in Figure 1a). This cavity is significantly sterically hindered and is primarily accessed by smaller metal cations intercalated at high stoichiometries.[22]

Previously published theoretical calculations predict CO_2 will preferentially bind to the Mo atoms on the surface of the CP cluster rather than the intercalants.[23,24] Intercalated metals located in the primary interstitial cavity, shaded blue in Figure 1a, coordinate to the sulfur atoms on the corners of the CP clusters. Through a chain electron transfer mechanism (Figure 1b), electron density is redistributed throughout the extended solid, originating from the intercalants and progressing through the hybridized Mo−S bond, resulting in a unique electron density localization at the predicted Mo binding site.[25] By choosing metal cations of varying electronegativity, indirect control over the electron density donation can be achieved. For instance, a more electronegative binding site is expected to have a stronger covalent interaction with the carbon of CO_2 leading to an increased binding energy according to the Sabatier principle, providing the residence time necessary for the absorbed CO_2 to undergo proton-coupled electron transfers (PCET) to higher-value products such as methanol.[5] Therefore, controlling the metal cation identity and stoichiometry would allow for direct modulation over electron transfer from the intercalants to the CP cluster through variation of the electronegativity of the metals.

Intercalation of a single-identity cation within the CP compositional framework, yielding a ternary periodic solid with the formula $M_yMo_6S_8$, has been extensively explored via electrochemical, solid-state, molten salt, and solution-based synthesis methods.[15,26−30] However, co-intercalation of two cations of differing identity, yielding a heterointercalant periodic solid, remains underexplored under all synthesis pathways. Heterointercalant frameworks of the formula $M_xM'_yMo_6S_8$ (M, M′ = Groups I/II, first-row transition metals, post transition metals; x, y = 0−4) have primarily been synthesized via electrochemical intercalation methods for multivalent battery cathode applications; however, electrochemical intercalation experiments have low catalyst yield and often compete against unfavorable electroplating reactions.[14,31−34] Therefore, a solid-state synthesis pathway that provides low-cost, high-yield accessibility of heterointercalant CP compositions is necessary. Through a robust synthetic pathway, it is then possible to investigate the electronic tunability of heterointercalant CP compositions and the impact on their catalytic activity.

In this work, we present a 5 min microwave-assisted synthesis of four heterointercalant CP materials ($Cu_xM_yMo_6S_8$, M = Cr, Mn, Fe, Ni; x, y = 1.5−2.5) for applications in electrochemical CO_2R. The electronic and structural properties of heterointercalant solids are characterized through refinement of the powder X-ray diffraction (PXRD) data, as well as X-ray photoelectron spectroscopy (XPS), high-resolution transmission electron microscopy (HR-TEM),

https://doi.org/10.1021/jacs.5c04404
J. Am. Chem. Soc. 2025, 147, 18155−18165

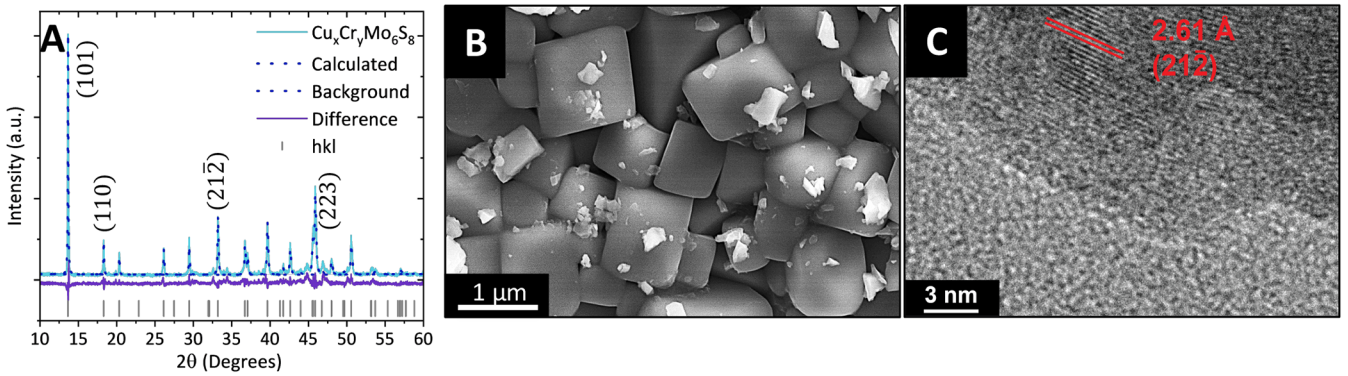

Figure 2. Refined PXRD diffractograms of experimentally synthesized $Cu_xCr_yMo_6S_8$ (A). Scanning electron micrographs for $Cu_xCr_yMo_6S_8$ depicting the expected CP cubic morphology (B). High-resolution transmission electron micrographs of $Cu_xCr_yMo_6S_8$ confirm lattice spacing agreement with calculated PXRD diffractograms (C).

selected-area electron diffraction (SAED), X-ray absorption near-edge structure (XANES), and extended X-ray absorption fine structure (EXAFS). Scanning electron microscopy (SEM) is used in combination with HR-TEM to confirm the expected morphology and particle size. Inductively coupled plasma optical emission spectroscopy (ICP-OES) was used to quantify the stoichiometry of each synthesized material. Finally, CO_2R was utilized as a probe reaction to analyze the electrocatalytic activity of all CP solids. Our previous results on the ternary $Cu_2Mo_6S_8$ solid indicate potential for methanol production on intercalated CP solids from CO_2R.[19] Herein, we demonstrate that control over the efficiency and selectivity of CP solids can be achieved through rapid synthetic methods that allow access to heterointercalant solids that contain an additional metal intercalated with Cu. Furthermore, the presence of a secondary cation with a different electronegativity and oxidation state resulted in electron transfer to the extended periodic CP solid distinguishable through spectroscopic analysis and an observed change in product selectivity for CO_2R. Intermediate analysis was examined through the aqueous reduction of formaldehyde, a proposed intermediate for CO_2R to methanol, and a tremendous increase in methanol production of up to 80% FE was observed on $Cu_xNi_yMo_6S_8$ and $Cu_xMn_yMo_6S_8$ solids. Through compositional modulation via intercalant identity, this work establishes fundamental composition−structure−function relationships. This study investigates a mechanism for redistributing electron density through chain electron transfer (as illustrated in Figure 1b) using CO_2R as a probe reaction. The goal is to develop a method for directly tuning extended periodic solids to influence the affinity of small-molecule catalytic intermediates. This approach could be generalized to other compositional spaces within similar periodic crystal solids, alike.

RESULTS AND DISCUSSION

Synthesis and Structural Characterization. Presented herein is the successful synthesis of four heterointercalant CP solids via microwave-assisted solid-state synthesis, a method previously utilized for the synthesis of binary and ternary CP solids.[18−20,25,28,35] The synthesis time for all heterointercalant solids was 5 min at ∼1000 °C, exactly half of the time necessary for the synthesis of ternary materials, namely, $Cu_2Mo_6S_8$ and $Fe_2Mo_6S_8$.[20] In previously published electrochemical intercalation of two or more cations, the primary interest was to elucidate the diffusion rate of cations within the framework under various applied potentials for battery cathode applications. It was determined through investigations into cyclic voltammetry that cation repulsion effects facilitated the diffusion of multiple cations throughout insertion and removal processes.[36] This phenomenon was most notably observed for the $Cu_xMg_yMo_6S_8$ framework in which the coupled diffusion of the two metal cations resulted in cyclic stability and effectively eliminated metal cation trapping within the cavities.[31,37] The observed decrease in synthesis time with the microwave-assisted method is hypothesized to be a result of improved diffusion of the reactants, similar to the previously observed synergy present in electrochemical intercalation experiments.[31] Structural confirmation of the synthesized materials was achieved via Rietveld refinement of the powder XRD data for each respective phase, shown in Figure 2a ($Cu_xCr_yMo_6S_8$ (Cu−Cr CP)) and Figure S1 ($Cu_xFe_yMo_6S_8$ (Cu−Fe CP), $Cu_xMn_yMo_6S_8$ (Cu−Mn CP) and $Cu_xNi_yMo_6S_8$ (Cu−Ni CP)). All heterointercalant solids exhibited a triclinic distortion from the rhombohedral $R\bar{3}H$ space group of binary Mo_6S_8 to the triclinic $P\bar{1}$ space group, as a result of electron transfer from the 3d orbitals of the intercalants to the orbitals 4d−3p hybridized Mo−S orbitals of the Mo_6S_8 clusters. As electron density is donated from the intercalants to the Mo_6S_8 cluster units, we observe a contraction of the Mo_6 octahedron, resulting in a cluster with greater cubic symmetry, as opposed to the previous trigonal antiprismatic. This is further observed in the XANES and EXAFS analysis in the subsequent sections. The electron density donation and contraction of the Mo_6 octahedron is the cause of the triclinic distortion from a trigonal to triclinic space group. An increase in the *a* lattice parameter and a decrease in the *c* lattice parameter is observed, indicating an elongation along the rotation axis of the extended periodic CP solid, consistent with a triclinic distortion away from the binary Mo_6S_8 rhombohedral symmetry (Table S1). Additionally, the lattice volume expansion of all heterointercalant solids is consistent with the occupation of the interstitial cavity with metal cations.[19] While refinement of the PXRD diffractogram confirms the cation occupation in the cavity, cation placement within position 1 or 2 cannot be confirmed due to the assumption presumed during refinement that the probability of the metal intercalants residing in one of the 12 inner and outer ring positions in the cavity (Figure 1a, intercalant positions site 1) was equiprobable. SEM images of $Cu_xCr_yMo_6S_8$ and the remaining CP solids are shown in Figures 2b and S2a−c, respectively, and demonstrate that the heterointercalant solids maintain the expected cubic morphol-

https://doi.org/10.1021/jacs.5c04404
J. Am. Chem. Soc. 2025, 147, 18155−18165

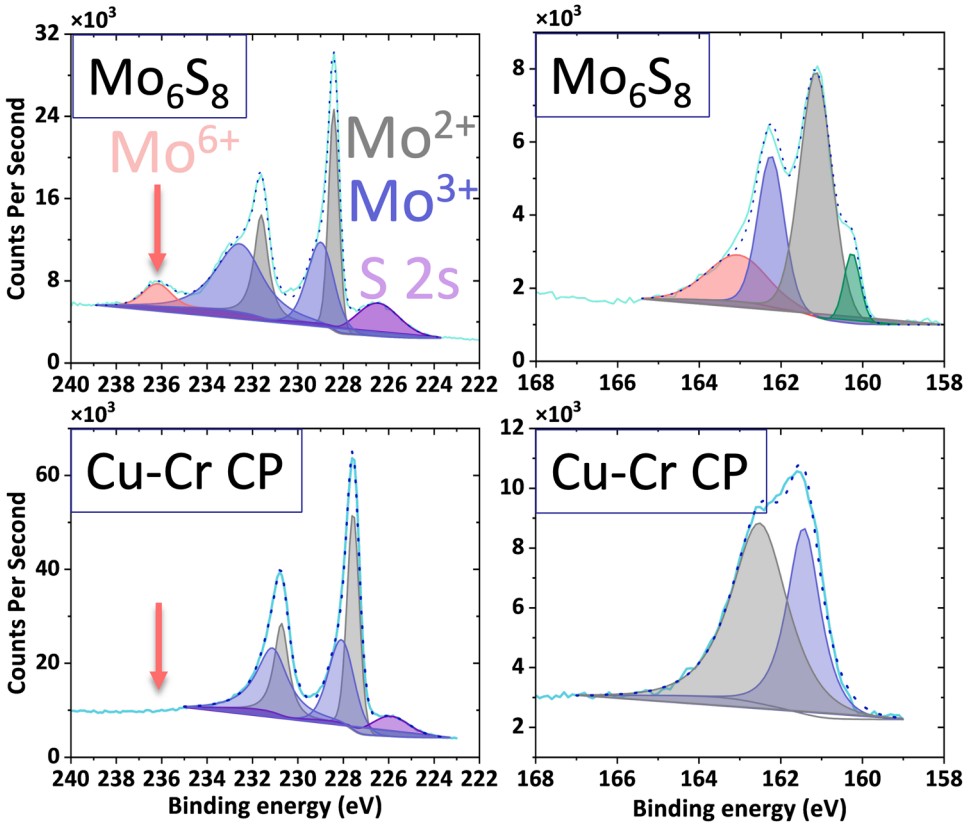

Figure 3. High-resolution XPS spectra of Mo 3d (A) and S 2p (B) for binary Mo_6S_8. High-resolution XPS spectra of Mo 3d (C) and S 2p (D) for $Cu_xCr_yMo_6S_8$. The loss of the Mo^{6+} oxidation state (orange in panel A) and the loss of the undercoordinated S peaks (orange and green in panel B) in the Cu−Cr CP solid indicate the electron transfer from the intercalants to the Mo_6S_8 cluster.

ogy of CP solids, with micrometer dimensions indicating bulk particle size. Furthermore, energy-dispersive X-ray (EDX) elemental mapping confirmed the homogeneity of metal cation distributions across all solids (Figures S3−S6), with experimental atomic percentages in good agreement with the expected concentrations. The stoichiometric concentrations of all solids was analyzed through ICP-OES (Table S2). However, we note that while the stoichiometry of intercalants is within the expected values, variations exist due to the bulk synthetic method utilized. Additionally, stoichiometric variation could be a result of the % error from the ICP-OES calibration curve (∼0−6%) and is presented in Table S2. PXRD analysis reveals no evidence of secondary phases despite the variations in metal intercalant stoichiometries. This may be attributed to the reaction of metal precursors with the fused silica reaction vessel.[38] Further structural confirmation was achieved through HR-TEM, shown in Figure 2c, in which labeled *d*-spacing values (red) align with characteristic CP peaks in the respective XRD diffractogram and SAED pattern shown in Figure S7. While confirmation of the extended periodic solid is achieved through structural characterization, spectroscopic analysis is necessary to investigate the chain electron transfer (Figure 1b) resulting from the metal cation occupation of the interstitial cavity.

Probing Chain Electron Transfer. According to the valence electron count (VEC) theory, each Mo_6S_8 unit in an unintercalated CP material is deficient by four electrons.[22] This assumption permits four monovalent cations capable of donating one electron to each cluster, or two divalent cations donating two electrons, to be intercalated. However, this restrictive assumption only considers the ionic interactions between intercalants and one cluster, without considering covalency or the additional surrounding clusters.[21,36,39] The expectation of an ionic interaction between the cluster and intercalants resulting in electron transfer would indicate instability through the occupation of the antibonding orbitals of a singular Mo_6S_8 cluster. With the inclusion of covalent interactions between the intercalants and the chalcogens of the clusters, higher intercalant content and stoichiometry is accessible. Higher stoichiometric compositions can be applied to enhance the understanding of the electron density redistribution from the intercalants to the expected Mo binding site.

Initial confirmation of electron density donation from the intercalants to the cluster was investigated through comparison of high-resolution XPS spectra, specifically the Mo 3d and S 2p regions, for all heterointercalant solids with unintercalated Mo_6S_8, shown in Figure 3. Comparisons between Mo_6S_8 and Cu−Cr CP were chosen as an example for the discussion due to the similarity of the high-resolution Mo 3d and S 2p scans across all heterointercalant solids. The Mo 3d and S 2p XPS spectra for Cu−Fe, Cu−Mn, and Cu−Ni CP solids are displayed in Figure S8. The binary Mo_6S_8 material contains peaks corresponding to 2+, 3+, and 6+ Mo oxidation states, shown in Figure 3a, at binding energies of 228.1, 229.2, and 236 eV, respectively.[14,18,40] The Mo^{6+} oxidation state, marked by the orange arrow in Figure 3a,c, is associated with either an unintercalated framework or a surface oxide and is lost upon intercalation of electron-donating cations in the CP cavities. Since all solids were subjected to a 4 keV Ar etch prior to XPS

https://doi.org/10.1021/jacs.5c04404
J. Am. Chem. Soc. 2025, 147, 18155−18165

data acquisition, the Mo^{6+} peak in binary Mo_6S_8 is not attributed to surface oxides but rather the absence of intercalants in the cavity. As electron density is redistributed to the Mo atoms upon intercalation, the unoccupied Mo 4d orbitals become filled, stabilizing the Mo_6 octahedron and leading to the loss of the Mo^{6+} oxidation-state peak and a shift to lower binding energies of the Mo L_3-edge in the heterointercalant solids (Figure S9). A shift to lower binding energies, from ∼2525 eV in binary Mo_6S_8 to ∼2523.2 eV for all heterointercalant solids, in the maxima of the first derivative in the Mo L_3-edge spectra is indicative of a more reduced species.[25] A shift to lower energies is also apparent in the binding energies of the 2+ and 3+ Mo oxidation states in the Cu−Cr CP Mo 3d spectra, further confirming reduced Mo (Figure 3c). In this case, the reduction is a direct result of electron density transfer from the 3d orbitals of the intercalants to the unoccupied hybridized 4d−3p orbitals of the surrounding Mo_6S_8 clusters.

The S 2p high-resolution XPS spectra of binary Mo_6S_8 shown in Figure 3b contains peaks at ∼163 and ∼160.5 eV correlated to undercoordinated sulfurs. The absence of the undercoordinated sulfur peaks in the S 2p spectra of Cu−Cr CP further confirms electron transfer from the intercalants to the Mo_6S_8 cluster.[41] The absence of the undercoordinated sulfur peaks in the XPS scans for all heterointercalant solids further indicates electron transfer from the intercalants to the framework due to the previously mentioned elimination of surface oxides post an Ar etch. Therefore, XPS has been employed to provide confirmation of the previously mentioned chain electron transfer reaction (Figure 1b) in which electron density is donated from the intercalants through the chalcogens at the corners of the individual clusters and redistributed to Mo atoms on the face of the cluster through the hybridized 4d−3p Mo−S bond.

As previously discussed, refinement of the PXRD data confirmed the occupation of the intercalants within the 12 equiprobable positions in the cavity. However, determination of cation placement within the outer and inner ring positions (Figure 4) would provide insights into the bonding motifs of the intercalants and thus the extent of chain electron transfer

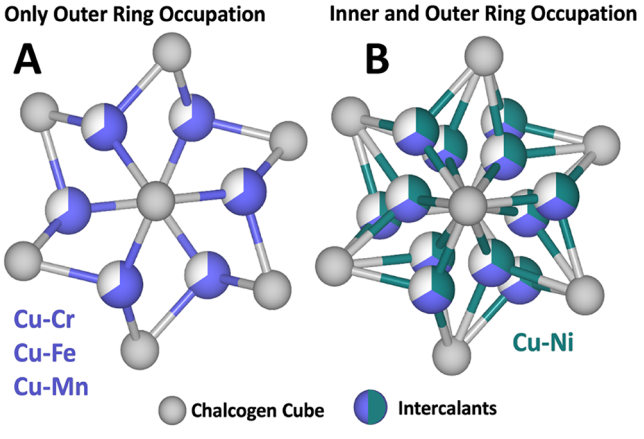

Figure 4. Intercalant occupation probability within the cavity for only position 2 outer ring occupation (A) and both position 1 inner ring and position 2 outer ring occupation (B). The Cu−Cr, Cu−Fe, and Cu−Mn CP solids exhibit only outer ring occupation, while the Cu−Ni solid shows signs of inner and outer ring intercalant occupation. All bonds between atoms are presumed covalent.

to the cluster. With respect to the oxidation state of each metal intercalant, high-resolution XPS spectra of the metals were acquired and a +1 oxidation for Cu and +2 oxidation for Cr, Fe, Mn, and Ni (Figure S10) were determined according to binding energies of previously published standard oxidation states.[14,42−45] It is assumed that Cu donates one electron equivalent to the surrounding clusters and Cr, Fe, Mn, and Ni donate two electron equivalents, as all reactant metals are expected to be in their ground state prior to synthesis. The high-resolution XPS spectra of the intercalated metals can be further assessed for peaks indicating occupation of the outer versus inner ring positions in the cavity through the presence of peaks at lower or higher binding energies.[40] The respective metal XPS spectra for Cu−Cr, Cu−Mn, and Cu−Fe CP contain only peaks corresponding to the expected oxidation state of each metal intercalant; however, additional peaks at lower binding energies are present in the Cu−Ni CP solid in the Cu 2p and Ni 2p high-resolution spectra (Figure S10d,h). The presence of peaks at lower binding energies in both the Ni 2p and Cu 2p spectra, for the Cu−Ni CP solid, compared to those corresponding to the respective +2 and +1 oxidation states, indicates the presence of a more reduced species.[6,45] However, the peaks at lower binding energies do not align with the expected peak position of metallic species with a 0 oxidation state. It can therefore be concluded that the reduced species could be a result of coordination within the cavity. The cations in position 2 (Figure 4a) denoted as the outer ring, have a stronger covalent interaction with the sulfurs of the clusters due to their inherent proximity, and are hence only coordinated to three sulfurs from the surrounding clusters. However, the inner ring positions are coordinated to the four surrounding Mo_6S_8 cluster units, potentially indicating a more reduced species. Based on these expectations, it can be hypothesized that the Cu−Ni CP solid contains reduced metal cations located in both positions 1 and 2 (Figure 4b), while the Cu−Cr, Cu−Mn, and Cu−Fe CP materials likely only have intercalants present in position 1 (Figure 4a). This result agrees with the expectation that smaller metal cations will delocalize from the center of the cavity at lower stoichiometries due to the stability of covalent bonding with the chalcogen of the clusters.[36] Further confirmation is present in the decrease in lattice volume observed in the Cu−Ni CP (Table S1) due to the decrease in steric crowding and thus minimized electrostatic repulsion with cations occupying the inner and outer rings, resulting in a contraction of the lattice parameters.[36]

Changes in the electronic structure between the binary and heterointercalant solids was confirmed through analysis of the S K-edge XANES region. Electron transfer from the intercalant combinations present in the cavity is further supported through an apparent depression of the S K-edge pre-edge XANES region, presented in Figure 5a. The pre-edge feature at 2471 eV is associated with a S 1s to S 3p excitation.[14] Depression of the pre-edge feature indicates occupation of the S 3p orbitals of the Mo_6S_8 cluster, as electron density is redistributed from intercalants to the empty sulfur orbitals. A clear depression is evident for all heterointercalant solids compared to binary Mo_6S_8 with a partial trend emerging for the Cu−Cr, Cu−Fe, and Cu−Ni CP materials. As the electronegativity of the second intercalant increases, a more pronounced depression is observed. The exception to this trend is Cu−Mn CP, which presents the most depressed pre-edge. However, given the Mn atoms are in a 2+ oxidation state, the resulting pre-edge depression seen in the Cu−Mn CP is

https://doi.org/10.1021/jacs.5c04404
J. Am. Chem. Soc. 2025, 147, 18155−18165

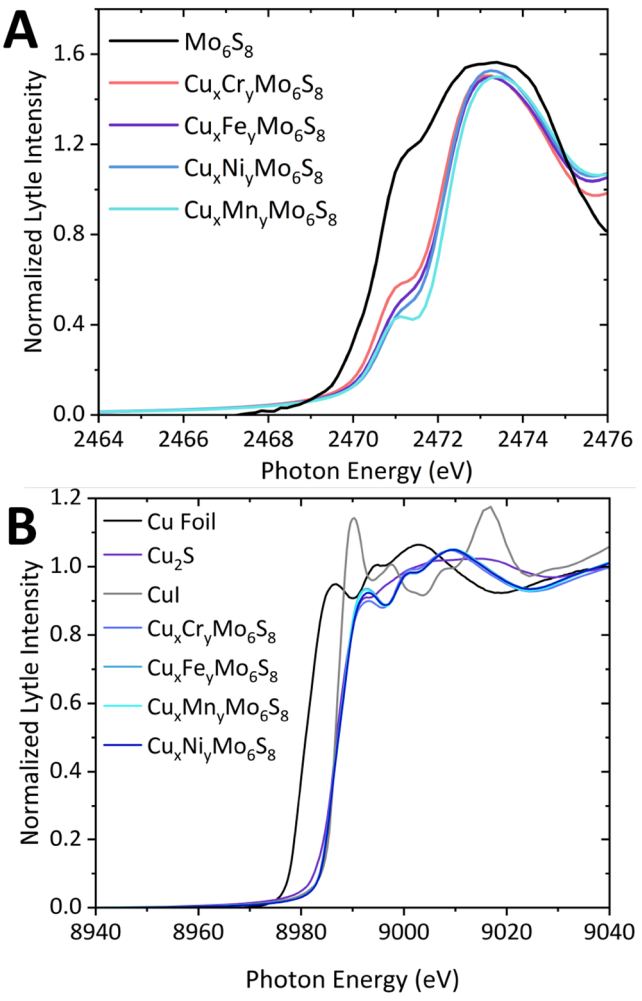

Figure 5. S K-edge data for all heterointercalant phases compared to binary Mo_6S_8 (A). A depression in the pre-edge feature of the S K-edge spectra is indicative of the transfer of electrons to the Mo_6S_8 cluster as a direct result of intercalation. Cu K-edge data for all heterointercalant CP solids compared to the Cu foil, Cu_2S, and CuI standards (B). The Cu K-edge can be utilized to understand coordination in the Cu cations compared to the CuI and Cu_2S standards.

due to the half-filled Mn d-orbital, which is hypothesized to have increased covalency and in turn increased electron transfer.[46] This effect in pre-edge feature depression highlights cation electronegativity as an additional means to modulate electron density redistribution, in addition to the aforementioned discussions of oxidation state and intercalant stoichiometry.

Investigation of the XANES spectra of the intercalant metal K-edges provides additional confirmation of the positioning of the intercalants in position 2. The Cu K-edge (Figure 5b) promotes the hypothesis that the Cu metal cations are three-coordinate within the cavity due to the alignment of the main rising edge with the Cu_2S standard. The two standards employed were CuI (four-coordinated Cu cations) and Cu_2S (three-coordinated Cu cations), both in a +1 oxidation state.[47,48] Given the alignment of the main rising edge of the heterointercalant solids with the rising edge of the Cu_2S materials, it can be presumed that the Cu intercalants exist in a three-coordinated environment, which corresponds to the outer ring positions. Additionally, all metal K-edges, shown in Figure S11, exhibit a pre-edge feature associated with a 1s to 4p shakedown process due to ligand (intercalant) to metal electron transfer (LMCT). The shakedown process consists of a relaxation of an electron from a ligand that fills the core hole of the metal as a result of the metal core electron excitation to the 4p orbital.[49]

The Cr, Ni, Mn, and Fe K-edges (Figure S11) further support the expectation for all intercalants to reside in position 2, with partial occupation of position 1 in the Cu−Ni CP. All intercalant K-edges exhibit a pre-edge feature corresponding to a 1s to 3d transition.[49] The depression of the pre-edge would correspond to the occupation of the 3d orbitals rendering the transition forbidden, similar to the S K-edge depression previously discussed. A shift in a main rising edge of a metal K-edge indicates a change in coordination and/or valency of the atom of interest.[50] In all metal K-edges shown in Figures 5b and S11, the main rising edge of the heterointercalant material is located at lower binding energies than the respective foil and standard, indicating a lower coordination and valency than the standards and metal foil. The metal K-edges additionally further support the oxidation states of the metal cations determined through the XPS shown in Figure S10.[51] Although first-row transition metals typically prefer tetrahedral and octahedral coordination due to their electron deficiency, it can be postulated that the intercalants are stabilized by electron transfer to the Chevrel-phase cluster and thus are capable of maintaining the expected three-coordinate configuration of position 2.

Intercalant-Induced Local Structural Distortion. To understand the structural distortion as a result of multiple cation intercalation, the Mo K-edge EXAFS region of all heterointercalant materials presented herein were compared to the binary Mo_6S_8 data previously published.[25] All Mo K-edge EXAFS data were confined to an R range of 1.2−3.8 Å to only consider near-neighbor contributions. The Fourier-transformed EXAFS data are shown in Figure 6, in which the magnitude and real components are presented. The normalized first derivative of the Mo K-edge is shown in Figure S12. Table S3 contains the extracted scattering paths and bond distances, and the extracted fitting parameters are tabulated in Tables S4−S7. The Mo K-edge fits in k-space corresponding to all heterointercalant solids are presented in Figure S13. Structural modifications to the cluster as a result of intercalants can be monitored through the $Mo-Mo_{intra}$ bond lengths, while contraction/expansion of the lattice can be observed through the $Mo-S_{inter}$ and $Mo-Mo_{inter}$ bond lengths (Figure S14). Contraction of the cluster because of intercalant electron transfer is calculated through cluster anisotropy, a metric used to quantify structural distortions. Percent anisotropy and error values are calculated according to eqs S4 and S5, respectively, and shown in Table S8.[52] Previously published experimental results calculated the anisotropy for the unintercalated Mo_6S_8 cluster as 8.85 ± 1.63%, with the Mo_6 cluster characterized as trigonal antiprismatic as opposed to octahedral owing to the larger difference between R_{long} and R_{short} distances in the $Mo-Mo_{intra}$ bond lengths.[25] A decrease in the percent anisotropy upon intercalation can be attributed to both electronic and geometric factors. The increased intercluster Mo−S bond distances can be ascribed to higher electron transfer from intercalants to the chalcogens, causing greater repulsion between Mo and S atoms (geometric factor). As the % anisotropy decreases, the difference between the $Mo-Mo_{intra}$ R_{short} and R_{long} decreases, resulting in a

https://doi.org/10.1021/jacs.5c04404
J. Am. Chem. Soc. 2025, 147, 18155−18165

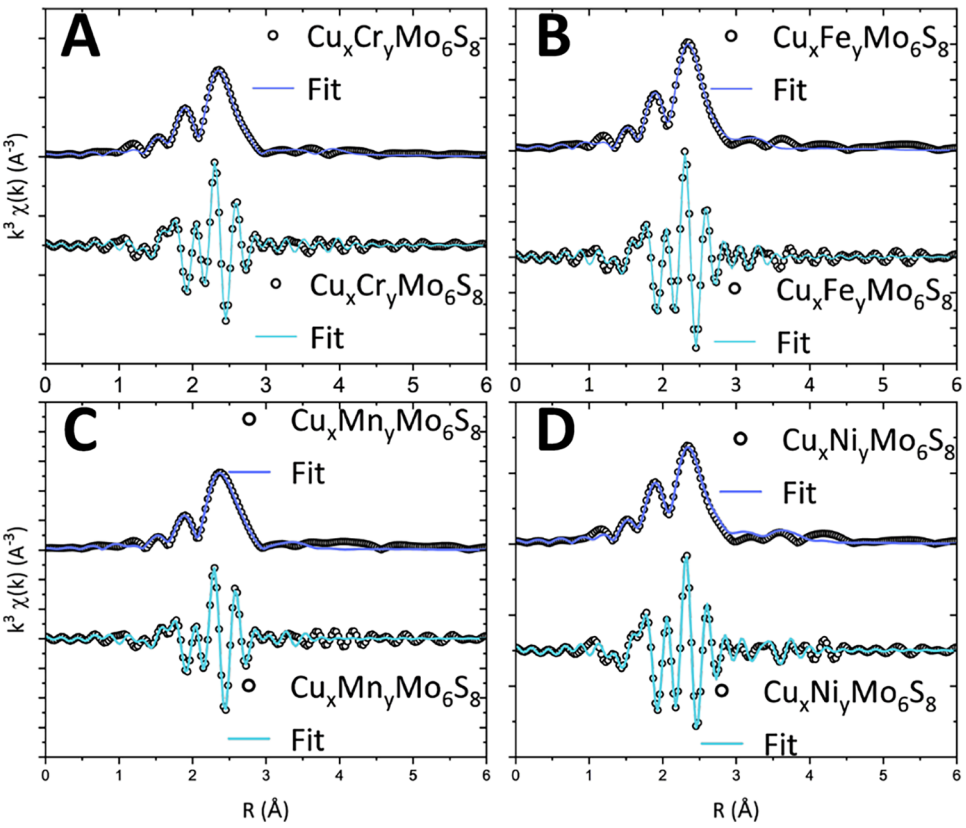

Figure 6. Mo K-edge FT-EXAFS data (circles) and fits (lines) with components of the FT $k^3\chi$(k) in nonphase corrected magnitude (top) and in real components (bottom) for $Cu_xCr_yMo_6S_8$ (A), $Cu_xFe_yMo_6S_8$ (B), $Cu_xMn_yMo_6S_8$ (C), and $Cu_xNi_yMo_6S_8$ (D).

coordination with greater octahedral symmetry as opposed to the trigonal prismatic coordination existing in the binary Mo_6S_8 cluster (electronic factor). The electronic structural changes observed agree with the triclinic distortion observed in the Rietveld refinement results of the PXRD as previously discussed and depicted in Figures 2a and 5a.

All heterointercalant solids included herein exhibit a significant decrease in cluster anisotropy as compared with binary Mo_6S_8, with Cu−Fe CP and Cu−Ni CP exhibiting the lowest percent anisotropy. This result indicates higher electron transfer from the intercalants to the CP framework, resulting in a structural distortion. With increased electron density redistribution into orbitals contributing to Mo−Mo bonding interactions, contraction of the octahedron is observed. This correlates well with the observed pre-edge depression of the XANES region of the S K-edge, indicating electron transfer to the chalcogen cube and in turn to the Mo_6 octahedron via Mo−S hybrid bonds. Previously published experimental results indicate that $Cu_2Mo_6S_8$ has a cluster anisotropy of 4.44 ± 1.64%. The insertion of an additional metal with Cu decreases the cluster anisotropy by a factor of ∼2, further indicating increased electron transfer to the cluster from the additional intercalant. Therefore, the synthesis of heterointercalant CP materials unlocks a new path to greater influence electron density localization on the Mo_6S_8 cluster and in turn the predicted Mo binding site.

Electrochemical Characterization. All heterointercalant solids presented herein were analyzed for the probe reaction of electrochemical CO_2R, in which a change in product selectivity was observed, as presented in Figure 7a. The low solubility of CO_2 in aqueous media allowed the competing hydrogen evolution reaction (HER) to prevail across all experiments. However, the product selectivity based on intercalant combinations present within the cavity of the CP framework is still evident when liquid product analysis is employed, specifically nuclear magnetic resonance (Figure S15). All four CP compositions resulted in altered product selectivity from two proton-coupled electron transfers (PCET), producing carbon monoxide (CO) and formate, up to six PCET to produce methanol. Previously published binding-energy calculations predict CO_2 prefers to adsorb to the Mo on the surface of the cluster for binary and ternary materials.[23] Translation of this phenomenon to heterointercalant solids can be considered through the increase in the level of electron transfer from the intercalants to the Mo atoms of the clusters via covalent interactions, as previously mentioned. By modulation of the electron density localization of the Mo atoms on the face of the clusters (the predicted active site), direct control over product selectivity can be achieved (ligand effect). The Sabatier principle postulates that an ideal binding strength would produce the specific products desired from CO_2R by stabilizing intermediates long enough for multiple PCET to occur but not too long to poison the surface.[5] With more electropositive cations co-intercalated with copper, namely Cr and Fe, products such as CO and formate are produced, indicating a weaker binding strength of CO_2 on the cluster as a result of only two PCET (Figure 8). The decreased binding strength could be a result of less electron density donation from the intercalants to the cluster and thus decreased stability of the intermediates resulting in lower PCET product formation. A preference toward the carbophilic pathway shown in Figure 8 would result in CO production

https://doi.org/10.1021/jacs.5c04404
J. Am. Chem. Soc. 2025, 147, 18155−18165

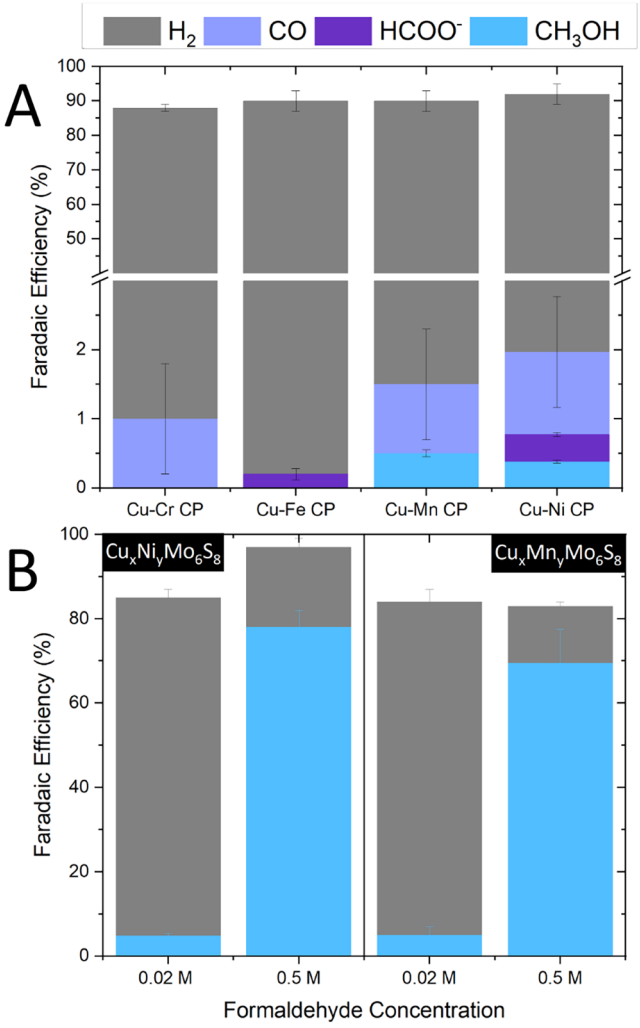

Figure 7. Faradaic efficiencies for CO_2 reduction at −0.5 V vs RHE on $Cu_xCr_yMo_6S_8$, $Cu_xFe_yMo_6S_8$, $Cu_xMn_yMo_6S_8$, and $Cu_xNi_yMo_6S_8$ (A). Faradaic efficiencies at −0.5 V vs RHE on $Cu_xNi_yMo_6S_8$ and $Cu_xMn_yMo_6S_8$ for aqueous electrochemical formaldehyde reduction at concentrations of 0.02 and 0.5M (B).

with two PCET with the carbon of CO_2 binding to Mo on the surface of the cluster; however, the oxophilic pathway favors formate production as the oxygens of CO_2 coordinates to the CP in a bidentate binding configuration.[39] Although HER prevailed across all materials, a change in reaction is implied between the Cu−Cr and Cu−Fe CP materials, as evident by the analysis of the product distribution.

In contrast, with more electronegative intercalants present, two or more products are observed, evident on the Cu−Mn and Cu−Ni CP materials. By increasing the electron density localization on the Mo atoms of the CP cluster, the CO_2 is stabilized and allowed to undergo further PCET yielding more valuable products, primarily methanol. In our previous work, we reported the production of methanol and formate on intercalated CP solids, namely, on $Cu_2Mo_6S_8$.[19] It was demonstrated that CP solids are capable of reducing CO_2 to methanol in aqueous environments with an increase in product selectivity observed under CO reduction experiments. CO studies were conducted to further evaluate the stability of intermediates on the surface, via the Faradaic Efficiency (FE) toward methanol. Given that the only difference of the heterointercalant solids presented herein with $Cu_2Mo_6S_8$ is the presence of an additional transition-metal intercalant in the cavity, similar trends under CO_2R conditions were expected. While similar products were observed, the inclusion of additional metals intercalated within the cavity resulted in a mechanistic shift from carbophilic to oxophilic pathways and toward higher PCET products depending on intercalants present. Furthermore, a preference for the carbophilic pathway to CO versus the oxophilic pathway to formate with the more electropositive intercalants could in part be due to the electron-withdrawing nature of early first-row transition metals that leads to less electron transfer to the CP cluster, resulting in the production of two PCET products. Catalyst stability was investigated via postelectrochemical experiment XPS scans (S16−S19), and catalyst composition and stability were confirmed through the comparison of the pre- and post-electrochemical experiments high-resolution XPS spectra of Mo 3d, S 2p, Cu 2p, and each respective intercalant for the heterointercalant solids.

Materials exhibiting the production of methanol were further evaluated for aqueous formaldehyde ([*CH_2O]) reduction to probe the carbophilic reaction pathway intermediates. According to the expected CO_2R pathway shown in Figure 8, [*CH_2O] is an expected intermediate in the reduction of CO_2 to methanol; therefore, it can be postulated that by

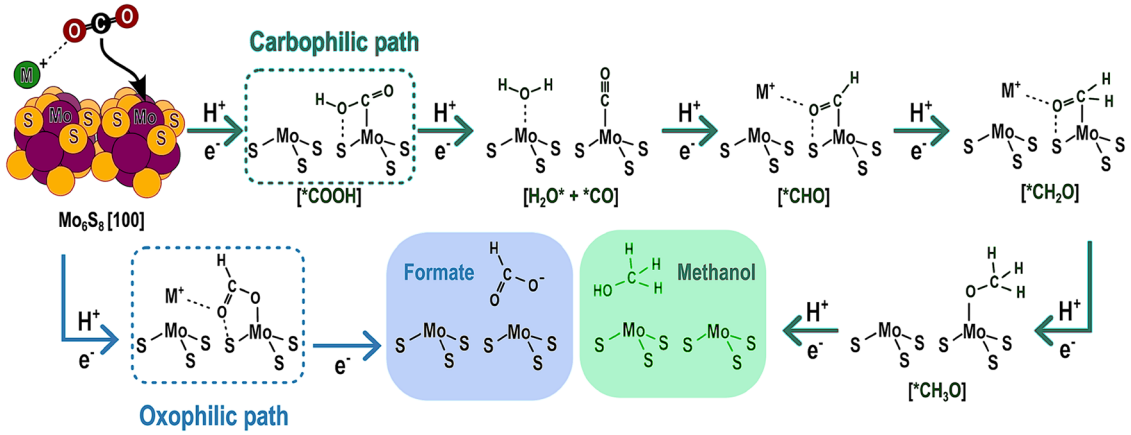

Figure 8. Mechanism of formate and methanol production over Chevrel-phase chalcogenides is believed to proceed via stepwise PCET. The carbophilic and oxophilic reaction pathways are separated, showing the distinct intermediates present for each respective product.

https://doi.org/10.1021/jacs.5c04404
J. Am. Chem. Soc. 2025, 147, 18155−18165

decreasing the six PCET necessary to produce methanol to two PCET from formaldehyde, there should be an increase in faradaic efficiency toward methanol.[53] This trend is evident on Cu−Ni and Cu−Mn CP solids, as shown in Figure 7b. Methanol production increased 5-fold with a production of 4−6% in 0.02 M formaldehyde solution and 60−80% in 0.5 M formaldehyde solution on both materials with only HER to compete, as shown in Figure 7b. Two well-known limitations of aqueous CO_2R are the low solubility of CO_2 leading to low concentrations in the electrolyte as well as poor diffusion to the surface of the catalyst in the static H-cell configuration used across all experiments. By reducing formaldehyde in the electrolyte, it is apparent that the Cu−Ni and Cu−Mn materials are exceptional at methanol production once the solubility and diffusion limitations are overcome.[54] The well-known Cannizarro reaction, a base-catalyzed reaction transforming an aldehyde to an alcohol, is present in the reduction of formaldehyde to methanol. To ensure proper product analysis of the Cu−Mn and Cu−Ni CP, dilute sulfuric acid was added to the post-electrolyte to stop the Cannizarro reaction from producing methanol at open-circuit potentials.[53,55] The apparent high FE toward methanol underscores the need for continued modulation of catalyst composition and structure to overcome the rate-limiting adsorption of CO_2 to the surface of the catalyst, as well as integration of additional experimental cell configurations. By unlocking additional synthesis pathways toward heterointercalant CP frameworks, we can indirectly control the stability of intermediates on the CP clusters. Continued research into microwave-assisted solid-state pathways to achieve CP catalyst compositions is needed to further understand the impact of the crystalline catalyst morphology and chain electron transfer for application in aqueous CO_2R.

CONCLUSIONS

In this work, we have accessed higher-stoichiometry heterointercalant CP solids via microwave-assisted solid-state synthesis. To the best of our knowledge, this study provides the first description of the synthesis and characterization of Cu−Cr, Cu−Fe, Cu−Mn, and Cu−Ni heterointercalant CP compositions with aqueous CO_2R to liquid and gaseous fuels as a probe reaction. The utilization of a low-cost, time-efficient synthesis technique via microwave assistance provides a robust pathway for the exploration of higher-stoichiometry CP compositions. A comprehensive characterization of the structural and electronic properties of the heterointercalant CP solids indicates preferential electron density donation corresponding to the cation combination present in the cavities of the extended CP solid. Further confirmation of electron density localization was evaluated via the analysis of the EXAFS and XANES regions of the chalcogen and metal K-edges. The electronic structure evaluation prompted an investigation of these materials for CO_2R to elucidate the effect of electron density localization on the product selectivity. Depending on the intercalant combination present in the CP solids, a change from the oxophilic to carbophilic product formation was observed. Furthermore, methanol production on Cu−Ni and Cu−Mn CP solids was confirmed, albeit at low efficiencies and current densities. However, under the reduction of the formaldehyde intermediate, FE toward methanol reached as high as 78% on Cu−Ni CP and 70% on Cu−Mn, indicating a rate-limiting reaction step that hinders the conversion of CO_2 to methanol. Continuing to build on the fundamental structural and electronic compositional foundations outlined in this and previous studies is of vital importance to further understand the impact of synthetic variability on small-molecule reactions, including CO_2R, HER, and nitrogen reduction.

ASSOCIATED CONTENT

Supporting Information

The Supporting Information is available free of charge at https://pubs.acs.org/doi/10.1021/jacs.5c04404.

Materials and experimental methods; rietveld refinement parameters; additional XRD, SEM, EDS, SAED, XPS, and TEM data; XAS Mo L3-edge; XAS metal K-edges; extracted EXAFS scattering paths and fitting parameters for all heterointercalant CP solids; anisotropy calculations; NMR analysis; post electrochemistry XPS spectra; product distributions at three potentials for CO_2R; and current densities and linear sweep voltammetry (PDF)

Accession Codes

Deposition Numbers 2430040−2430043 contain the supplementary crystallographic data for this paper. These data can be obtained free of charge via the joint Cambridge Crystallographic Data Centre (CCDC) and Fachinformationszentrum Karlsruhe Access Structures Service.

AUTHOR INFORMATION

Corresponding Author

Jesús M. Velázquez − *Department of Chemistry, University of California, Davis, California 95616, United States; Department of Chemical Engineering and Department of Agricultural and Environmental Chemistry, University of California, Davis, California 95616, United States;* orcid.org/0000-0003-2790-0976; Email: jevelazquez@ucdavis.edu

Authors

Konstantina G. Mason − *Department of Chemistry, University of California, Davis, California 95616, United States;* orcid.org/0009-0008-8116-9196

Natalia Mosqueda − *Department of Mechanical Engineering, University of California, Davis, California 95616, United States*

S. Avery Vigil − *Department of Chemistry, Duke University, Durham, North Carolina 27708, United States;* orcid.org/0009-0002-5150-0470

Paola N. Del Pozo-Gonzalez − *Department of Chemistry, University of Puerto Rico Humacao, Humacao 00791, Puerto Rico*

Saxton Feiner − *Department of Materials Science and Engineering, University of California, Davis, California 95616, United States*

Kingston P. Robinson − *Department of Chemistry, University of California, Davis, California 95616, United States*

Jenna M. Ynzunza − *Department of Chemical Engineering, University of California, Davis, California 95616, United States*

Ankita Kumari − *Department of Agricultural and Environmental Chemistry, University of California, Davis, California 95616, United States*

Rose E. Smiley − *Department of Chemistry, University of California, Davis, California 95616, United States*

Erika La Plante − *Department of Materials Science and Engineering, University of California, Davis, California 95616, United States;* orcid.org/0000-0002-5273-9523
George Agbeworvi − *Department of Chemistry, Texas A&M University, College Station, Texas 77843, United States*
Ivan A. Moreno-Hernandez − *Department of Chemistry, Duke University, Durham, North Carolina 27708, United States;* orcid.org/0000-0001-6461-9214

Complete contact information is available at: https://pubs.acs.org/10.1021/jacs.5c04404

Notes

The authors declare no competing financial interest.

■ ACKNOWLEDGMENTS

J.M.V. thanks the National Science Foundation for support through the Faculty Early Career Development Program (DMR-2044403). K.M. and J.M.V. acknowledge support from the University of California Office of the President and the National Laboratory Research Fees Program with Award L22CR4468 (materials characterization, PXRD, SEM, EDS). J.M.V. thanks the support of the Center for Closing the Carbon Cycle, an Energy Frontier Research Center funded by the U.S. Department of Energy, Office of Science, Basic Energy Sciences, under Award Number DE-SC0023427 (electroanalytical characterization, GC-TCD, NMR, materials characterization, XAS). Additionally, J.M.V. also acknowledges funding support from the Camille Dreyfus Teacher-Scholar Awards Program (TC-22-096), the Alfred P. Sloan Foundation Award (FG-2023-203903), and the Cottrell Scholars Program supported by the Research Corporation for Science Advancement (RCSA 26780). Use of the Stanford Synchrotron Radiation Lightsource, SLAC National Accelerator Laboratory, is supported by the U.S. Department of Energy, Office of Science, Office of Basic Energy Sciences under Contract No. DEAC02-765F00515. XPS analysis at UC Davis was conducted in the Advanced Materials Characterization and Testing (AMCaT) Laboratory supported by the National Science Foundation (DMR-1828238). P.N.D. was funded for summer research through the National Science Foundation ChemEnergy Research Undergrad Experience Program (CHE1950933). N.M. was funded for summer research through the National Science Foundation LSAMP/CAMP Research Undergrad Experience Program. K.P.R. acknowledges funding from the NSF Graduate Research Fellowship Program.

■ REFERENCES

(1) van der Zande, R. M.; Achlatis, M.; Bender-Champ, D.; Kubicek, A.; Dove, S.; Hoegh-Guldberg, O. Paradise lost: End-of-century warming and acidification under business-as-usual emissions have severe consequences for symbiotic corals. *Global Change Biol.* **2020**, *26* (4), 2203−2219.
(2) Karnauskas, B. K.; Miller, L. S.; Schapiro, C. A. Fossil Fuel Combustion Is Driving Indoor CO2 Toward Levels Harmful to Human Cognition. *GeoHealth* **2020**, *4* (5), No. e2019GH000237, DOI: 10.1029/2019gh000237.
(3) Svanberg, M.; Ellis, J.; Lundgren, J.; Landälv, I. Renewable methanol as a fuel for the shipping industry. *Renewable Sustainable Energy Rev.* **2018**, *94*, 1217−1228.
(4) Zhang, X.; Guo, S.-X.; Gandionco, K. A.; Bond, A. M.; Zhang, J. Electrocatalytic carbon dioxide reduction: from fundamental principles to catalyst design. *Mater. Today Adv.* **2020**, *7*, No. 1000074.
(5) Ooka, H.; Huang, J.; Exner, S. K. The Sabatier Principle in Electrocatalysis: Basics, Limitations, and Extensions. *Front. Energy Res.* **2021**, *9*, No. 654460.
(6) Guo, L.; Zhou, J.; Liu, F.; Meng, X.; Ma, Y.; Hao, F.; Xiong, Y.; Fan, Z. Electronic Structure Design of Transition Metal-Based Catalysts for Electrochemical Carbon Dioxide Reduction. *ACS Nano* **2024**, *18* (14), 9823−9851.
(7) Chen, T.; Foo, C.; Tsang, E. C. S. Interstitial and substitutional light elements in transition metals for heterogeneous catalysis. *Chem. Sci.* **2021**, *12* (2), 517−532.
(8) Chevrel, R.; Sergent, M.; Prigent, J. Sur de nouvelles phases sulfurées ternaires du molybdène. *J. Solid State Chem.* **1971**, *3* (4), 515−519.
(9) Tsubota, T.; Ohtaki, M.; Eguchi, K. Thermoelectric Properties of Chevrel-Type Sulfides AMo6S8. (A = Fe, Ni, Ag, Zn, Sn, Pb, Cu). *J. Ceram. Soc. Jpn.* **1999**, *107* (1248), 697−701.
(10) Ohta, M.; Yamamoto, A.; Obara, H. Thermoelectric Properties of Chevrel-Phase Sulfides M x Mo6S8 (M: Cr, Mn, Fe, Ni). *J. Electron. Mater.* **2010**, *39* (9), 2117−2121.
(11) Caillat, T.; Fleurial, J.-P.; Snyder, G. J. Potential of Chevrel phases for thermoelectric applications. *Solid State Sci.* **1999**, *1* (7-8), 535−544.
(12) Gilmore, T.; Rochester, J.; Sumption, M.; Gouma, P.-I. Intercalation based synthesis of Chevrel phase superconductors. *J. Mater. Sci.* **2024**, *59* (26), 11880−11892.
(13) Vaishnava, P. P.; Kimball, W. C.; Matykiewicz, L. J.; Fradin, Y. F.; Shenoy, K. G.; Montano, A. P. Extended x-ray-absorption fine-structure observation of collinear ordering of Fe-Sn-Fe atoms in the Chevrel-phase superconductorSnFe0.05Mo6S8. *Phys. Rev. B* **1986**, *34* (7), No. 4599.
(14) Ritter, A. K.; Mason, G. K.; Yew, S.; Perryman, T. J.; Ortiz-Rodríguez, C. J.; Singstock, R. N.; Bille, W. A. B.; Musgrave, B. C.; Velázquez, M. J. Electrochemical control over stoichiometry via cation intercalation into Chevrel-phase sulphides (CuxMo6S8, x = 1−3). *J. Mater. Chem. A* **2024**, *12* (12), 7199−7206.
(15) Cho, J.-H.; Aykoi, M.; Kim, S.; Ha, J.-H.; Wolverton, C.; Chung, K. Y.; Kim, K.-B.; Cho, B.-W. Controlling the Intercalation Chemistry to Design High-Performance Dual-Salt Hybrid Rechargeable Batteries. *J. Am. Chem. Soc.* **2014**, *136* (46), 16116−16119.
(16) Singstock, N. R.; Musgrave, C. B. How the Bioinspired Fe2Mo6S8 Chevrel Breaks Electrocatalytic Nitrogen Reduction Scaling Relations. *J. Am. Chem. Soc.* **2022**, *144* (28), 12800−12806.
(17) Singstock, N. R.; Ortiz-Rodríguez, C. J.; Perryman, T. J.; Sutton, C.; Velázquez, M. J.; Musgrave, B. C. Machine Learning Guided Synthesis of Multinary Chevrel Phase Chalcogenides. *J. Am. Chem. Soc.* **2021**, *143* (24), 9113−9122.
(18) Ortiz-Rodríguez, C. J.; Singstock, R. N.; Perryman, T. J.; Hyler, P. F.; Jones, J. S.; Holder, M. A.; Musgrave, B. C.; Velázquez, M. J. Stabilizing Hydrogen Adsorption through Theory-Guided Chalcogen Substitution in Chevrel-Phase Mo_6X_8 (X=S, Se, Te) Electrocatalysts. *ACS Appl. Mater. Interfaces* **2020**, *12* (32), 35995−36003.
(19) Perryman, T. J.; Ortiz-Rodríguez, C. J.; Jude, W. J.; Hyler, P. F.; Davis, C. R.; Mehta, A.; Kulkarni, R. A.; Patridge, J. C.; Velázquez, M. J. Metal-promoted Mo6S8 clusters: a platform for probing ensemble effects on the electrochemical conversion of CO2 and CO to methanol. *Mater. Horiz.* **2020**, *7* (1), 193−202.
(20) Perryman, J. T.; Hyler, P. F.; Ortiz-Rodríguez, C. J.; Mehta, A.; Kulkarni, R. A.; Velázquez, M. J. X-ray absorption spectroscopy study of the electronic structure and local coordination of 1st row transition metal-promoted Chevrel-phase sulfides. *J. Coord. Chem.* **2019**, *72* (8), 1322−1335.
(21) Levi, E.; Gershinsky, G.; Isnard, O. Crystallography of Chevrel Phases, MMo6T8 (M = Cd, Na, Mn, and Zn, T = S, Se) and Their Cation Mobility. *Inorg. Chem.* **2009**, *48* (18), 8751−8758.
(22) Fischer, O.; Maple, M. B. *Superconductivity in Ternary Compounds I*; Springer, 1982.
(23) Liu, P.; Choi, Y.; Yang, Y.; White, M. G. Methanol Synthesis from H2 and CO2 on a Mo6S8 Cluster: A Density Functional Study. *J. Phys. Chem. A* **2010**, *114* (11), 3888−3895.

(24) Patterson, M. J.; Lightstone, J. M.; White, M. G. Structure of Molybdenum and Tungsten Sulfide $M_xS_y^+$ Clusters: Experiment and DFT Calculations. *J. Phys. Chem. A* **2008**, *112* (47), 12011−12021.
(25) Hyler, F. P.; Bille, B. A. W.; Bille, W. A. B.; Ortíz-Rodríguez, C. J.; Sanz-Matias, A.; Roychoudhury, S.; Perryman, T. J.; Patridge, J. C.; Singstock, R. N.; Musgrave, B. C.; Prendergast, D. X-ray absorption spectroscopy insights on the structure anisotropy and charge transfer in Chevrel Phase chalcogenides. *Phys. Chem. Chem. Phys.* **2022**, *24* (28), 17289−17294.
(26) Lancry, E.; Levi, E.; Mitelman, A.; Malovany, S.; Aurbach, D. Molten salt synthesis (MSS) of Cu2Mo6S8—New way for large-scale production of Chevrel phases. *J. Solid State Chem.* **2006**, *179* (6), 1879−1882.
(27) Gupta, G.; Gupta, R.; Gupta, A.; Kumar, D. Electrochemical studies and diffusion kinetics in the Chevrel phase (Mo6S8) for rechargeable Mg batteries. *J. Phys. D: Appl. Phys.* **2024**, *57* (48), No. 485503.
(28) Murgia, F.; Antitomaso, P.; Stievano, L.; Monconduit, L.; Berthelot, R. Express and low-cost microwave synthesis of the ternary Chevrel phase $Cu_2Mo_6S_8$ for application in rechargeable magnesium batteries. *J. Solid State Chem.* **2016**, *242*, 151−154.
(29) Cheng, Y.; Parent, L. R.; Shao, Y.; Wang, C.; Sprenkly, V. L.; Li, G.; Liu, J. Facile Synthesis of Chevrel Phase Nanocubes and Their Applications for Multivalent Energy Storage. *Chem. Mater.* **2014**, *26* (17), 4904−4907.
(30) Fradin, F. Y.; Downey, J. W. Crystallography of mixed Chevrel phases. *Mater. Res. Bull.* **1979**, *14* (12), 1525−1528.
(31) Levi, E.; Mitelman, A.; Aurbach, D.; Brunelli, M. Structural Mechanism of the Phase Transitions in the Mg−Cu−Mo6S8 System Probed by ex Situ Synchrotron X-ray Diffraction. *Chem. Mater.* **2007**, *19* (21), 5131−5142.
(32) Li, H.; Ichitsubo, T.; Yagi, S.; Matsubara, E. Constructing metal-anode rechargeable batteries utilizing concomitant intercalation of Li−Mg dual cations into Mo_6S_8. *J. Mater. Chem. A* **2017**, *5* (7), 3534−3540.
(33) Niu, H. J.; Morley, N. A.; Hampshire, D. P. Chevrel phase (Pb/sub 1-x/Cu/sub 1.8x/)Mo/sub 6/S/sub 8/ with a mixed structure and high critical parameters. *IEEE Trans. Appl. Supercond.* **2001**, *11* (1), 3619−3622.
(34) Mckinnon, R. W.; Dahn, R. J.; Jui, H. C. C. LixCuyMo6S8: a pseudoternary intercalation compound. *J. Phys. C: Solid State Phys.* **1985**, *18* (23), 4443−4458.
(35) Lilova, K.; Perryman, T. J.; Singstock, R. N.; Abramchuk, M.; Subramani, T.; Lam, A.; Yoo, R.; Ortiz-Rodríguez, C. J.; Musgrave, B. C.; Navrotsky, A.; Velázquez, J. M. A Synergistic Approach to Unraveling the Thermodynamic Stability of Binary and Ternary Chevrel Phase Sulfides. *Chem. Mater.* **2020**, *32* (16), 7044−7051.
(36) Levi, E.; Gershinsky, G.; Aurbach, D.; Isnard, O.; Ceder, G. New Insight on the Unusually High Ionic Mobility in Chevrel Phases. *Chem. Mater.* **2009**, *21* (7), 1390−1399.
(37) Choi, S.-H.; Kim, J.-S.; Woo, S.-G.; Cho, W.; Choi, S. Y.; Choi, J.; Lee, K.-T.; Park, M.-S.; Kim, Y.-J. Role of Cu in Mo_6S_8 and Cu Mixture Cathodes for Magnesium Ion Batteries. *ACS Appl. Mater. Interfaces* **2015**, *7* (12), 7016−7024.
(38) Landry, C. C.; Lockwood, J.; Barron, A. R. Synthesis of Chalcopyrite Semiconductors and Their Solid Solutions by Microwave Irradiation. *Chem. Mater.* **1995**, *7* (4), 699−706.
(39) Liu, C.; Liu, P. Mechanistic Study of Methanol Synthesis from CO2 and H2 on a Modified Model Mo6S8 Cluster. *ACS Catal.* **2015**, *5* (2), 1004−1012.
(40) Richard, J.; Benayad, A.; Colin, J.-F.; Martinet, S. Charge Transfer Mechanism into the Chevrel Phase Mo_6S_8 during Mg Intercalation. *J. Phys. Chem. C* **2017**, *121* (32), 17096−17103.
(41) Yvon, K.; Paoli, A. Charge transfer and valence electron concentration in Chevrel phases. *Solid State Commun.* **1977**, *24* (1), 41−45.
(42) Crêpellière, J.; Popa, L. P.; Bahlawane, N.; Leturcq, R.; Werner, F.; Siebentritt, S.; Lenoble, D. Transparent conductive $CuCrO_2$thin films deposited by pulsed injection metal organic chemical vapor deposition: up-scalable process technology for an improved transparency/conductivity trade-off. *J. Mater. Chem. C* **2016**, *4* (19), 4278−4287.
(43) Li, P.; Xuan, Y.; Jiang, B.; Zhang, S.; Xia, C. Hollow La0.6Sr0.4Ni0.2Fe0.75Mo0.05O3-δ electrodes with exsolved FeNi3 in quasi-symmetrical solid oxide electrolysis cells for direct CO2 electrolysis. *Electrochem. Commun.* **2022**, *134*, No. 107188.
(44) Chinnadurai, D.; Selvaraj, R. A.; Rajendiran, R.; Kumar, R. G.; Kim, H.-J.; Viswanathan, K. K.; Prabakar, K. Inhibition of Redox Behaviors in Hierarchically Structured Manganese Cobalt Phosphate Supercapacitor Performance by Surface Trivalent Cations. *ACS Omega* **2018**, *3* (2), 1718−1725.
(45) Xiong, D.; Li, W.; Liu, L. Vertically Aligned Porous Nickel(II) Hydroxide Nanosheets Supported on Carbon Paper with Long-Term Oxygen Evolution Performance. *Chem. − Asian J.* **2017**, *12* (5), 543−551.
(46) Goodenough, J. B. Perspective on Engineering Transition-Metal Oxides. *Chem. Mater.* **2014**, *26* (1), 820−829.
(47) Ivanova, T. M.; Maslakov, K. I.; Sidorov, A. A.; Kiskin, M. A.; Linko, R. V.; Savilov, S. V.; Lunin, V. V.; Eremenko, I. L. XPS detection of unusual Cu(II) to Cu(I) transition on the surface of complexes with redox-active ligands. *J. Electron Spectrosc. Relat. Phenom.* **2020**, *238*, No. 146878.
(48) Kumar, P.; Nagarajan, R.; Sarangi, R. Quantitative X-ray absorption and emission spectroscopies: electronic structure elucidation of Cu2S and CuS. *J. Mater. Chem. C* **2013**, *1* (13), 2448−2454.
(49) Baker, M. L.; Mara, W. M.; Yan, J. J.; Hodgson, O. K.; Hedman, B.; Solomon, I. E. K- and L-edge X-ray absorption spectroscopy (XAS) and resonant inelastic X-ray scattering (RIXS) determination of differential orbital covalency (DOC) of transition metal sites. *Coord. Chem. Rev.* **2017**, *345*, 182−208.
(50) Tromp, M.; Moulin, J.; Reid, G.; Evans, J. In *Cr K-Edge XANES Spectroscopy: Ligand and Oxidation State Dependence — What is Oxidation State?*, AIP Conference Proceedings; AIP Publishing, 2007.
(51) Lou, D.; Yutronkie, J. N.; Oyarzabal, I.; Wang, L.-F.; Adak, A.; Nadurata, L. V.; Diego, R.; Suturina, A. E.; Mailman, A.; Dechambenoit, P.; et al. Self-Assembled Tetranuclear Square Complex of Chromium(III) Bridged by Radical Pyrazine: A Molecular Model for Metal−Organic Magnets. *J. Am. Chem. Soc.* **2024**, *146* (29), 19649−19653.
(52) Levi, E.; Aurbach, D. Chevrel Phases, MxMo6T8 (M = Metals, T = S, Se, Te) as a Structural Chameleon: Changes in the Rhombohedral Framework and Triclinic Distortion. *Chem. Mater.* **2010**, *22* (12), 3678−3692.
(53) Birdja, Y. Y.; Koper, M. T. M. The Importance of Cannizzaro-Type Reactions during Electrocatalytic Reduction of Carbon Dioxide. *J. Am. Chem. Soc.* **2017**, *139* (5), 2030−2034.
(54) Sun, Z.; Ma, T.; Tao, H.; Fan, Q.; Han, B. Fundamentals and Challenges of Electrochemical CO2 Reduction Using Two-Dimensional Materials. *Chem* **2017**, *3* (4), 560−587.
(55) Wawrzyniak, A.; Koper, M. T. M. Electrocatalytic CO2 Reduction to Methanol on Pt(111) Modified with a Pd Monolayer. *ACS Catal.* **2025**, *15*, 1514−1521.

https://doi.org/10.1021/jacs.5c04404
J. Am. Chem. Soc. 2025, 147, 18155−18165